Photocatalytic transformation of the antipsychotic drug risperidone in aqueous media on reduced graphene oxide—TiO$_2$ composites

P. Calza [a], C. Hadjicostas [b], V.A. Sakkas [b,*], M. Sarro [a], C. Minero [a], C. Medana [c], T.A. Albanis [b]

[a] Department of Chemistry and NIS centre, University of Torino, via P. Giuria 7, 10125 Torino, Italy
[b] Department of Chemistry, University of Ioannina, Ioannina 45110, Greece
[c] Department of Molecular Biotechnology and Health Sciences, University of Torino, via P. Giuria 5, 10125 Torino, Italy

ABSTRACT

In the present study reduced graphene oxide—TiO$_2$ composites were synthesized at two different ratios (1:10 and 1:5) through a hydrothermal method using graphene oxide and commercial P25 as starting materials. Scanning Electron Microscopy (SEM), Transmission Electron Microscopy (TEM), X-ray diffraction (XRD), Fourier transform infrared spectroscopy (FTIR), BET surface area and ultraviolet–visible (UV–vis) absorption spectroscopy were employed to investigate the morphology and properties of the produced composites. The photocatalytic performance of TiO$_2$–rGO catalysts was evaluated under artificial solar light and visible light in distilled water, as well as, different surface waters (at natural pH) with respect to risperidone (antipsychotic drug) degradation. Irrespectively of the irradiated aqueous matrix, the photocatalytic efficiency of the tested composite materials under simulated solar light and visible light irradiation was higher compared to bare TiO$_2$–P25 (reference catalyst).

The identification of intermediate compounds, the assessment of mineralization and the evaluation of toxicity were performed as well. LC/HRMS was brought to bear in assessing the temporal course of the photocatalyzed process. Along with risperidone decomposition, the formation of twenty intermediate compounds (TPs) occurred in the presence of TiO$_2$. Irradiation of risperidone in the presence of the hybrid material resulted in the identification of thirty-four TPs. The transformation of risperidone progressed through the formation of compounds more harmful than the drug itself, as assessed by the measurement of acute toxicity, evaluated using the *Vibrio fischeri* bacteria test. When employing TiO$_2$–rGO, all the identified transformation products were quicker degraded compared to TiO$_2$–P25. At the same time both the reduction of toxicity and mineralization were faster achieved than with bare TiO$_2$–P25.

© 2015 Elsevier B.V. All rights reserved.

1. Introduction

Risperidone (4-[2-[4-(6-fluorobenzo[d]oxazol-3-il)-1-piperidil]ethyl]-3-methyl-2,6-diazabicycle [4.4.0]deca-1,3-dien-5-one) is a benzisoxazole antipsychotic drug, mainly used to treat schizophrenia and other psychiatric illnesses.

Risperidone (RS) is easily and well absorbed by the human body while it is metabolized to 9-hydroxy-risperidone that has a similar pharmacological activity as RS [1]. One week after oral administration, RS and its major metabolite are excreted 70% in the urine and, to a much lesser extent, in the faeces (14%) [2]. Both chemicals that form the active antipsychotic fraction have been detected in human breast milk [3].

Risperidone's production and use as an antipsychotic drug may result in its release to the environment [1]. However, information concerning the fate and environmental behavior of RS (partitioning, transport, degradation, interaction with other environmental media) is still scarce. As regards the aquatic environment, RS does not contain chromophores that absorb at wavelengths >290 nm and, therefore, is not expected to be susceptible to direct photolysis by sunlight [1]. In addition, volatilization from water surfaces is not expected to be an important fate process [1]. At the same time, hydrolysis is not expected to be an important environmental fate process since this compound lacks functional groups that hydrolyze under environmental conditions [1].

Currently, studies on the environmental transformation of RS are scarce. A recent study carried out in the Santorini Island (Aegean Sea, Greece), reported the occurrence of RS as well as its metabolite (9-hydroxy-risperidone) in influent and effluent wastewaters up to concentration levels of 3.2 and 11.8 ng L^{-1}, respectively [4]. Although the concentration in the aquatic environment is too low

to pose a very acute risk according to RS Safety Data Sheet (in accordance with Regulation (EC) No. 1907/2006), RS is hazardous to the aquatic environment (Aquatic Chronic 2, H411, R51/53, N, T) [5]. Therefore, a crucial need for more enhanced technologies that can reduce its presence in the environment has become evident.

HPLC/MS technique is the more suitable technique to analyze RS in different matrices [6–8].

Advanced oxidation processes, above all photocatalytic process, are frequently used to treat emerging pollutants, and achieve their complete mineralization [9–13]. The degradation of pollutants by means of TiO_2 is well documented in the literature [14–15]. However, conventional TiO_2 photocatalysis has barriers in practical remediation of organic pollutants due to the low efficiency in sunlight absorption [16].

In exploring approaches to increase the efficiency of TiO_2 photocatalyst, graphene based nanocomposite systems have been utilized [17–24]. The great interest on the employment of graphene/graphene derivatives based TiO_2 both in terms of energy production as well as environmental remediation is attributed to the higher light absorption ability of the composites, as well as, the reduced recombination rates of electron-hole pairs, further improving the photocatalytic efficiency [25,26].

In the present work reduced graphene oxide—TiO_2 photocatalysts were synthesized at two different ratios (1:5 and 1:10, named, TiO_2–rGO_{20}, TiO_2–rGO_{10}) through a hydrothermal method using graphene oxide and commercial P25 as starting materials. After characterization of the synthesized composites (morphological and textural characteristics, crystal structure and optical properties), their photocatalytic activities were assessed through the photodegradation of RS under a variety of experimental conditions, such as, different aqueous matrices (distilled, tap, river and lake water) under artificial solar light and visible light. According to our knowledge this is the first time that the photocatalyzed transformation of RS is examined. Moreover, we explore here the transformation of an RS using heterogeneous photocatalysis by assessing the mechanism of transformation and the toxicity related to the drug and to its transformation products.

2. Experimental

2.1. Material and reagents

Sulfuric acid (>95%), potassium permanganate (99%), hydrogen peroxide (30%), hydrochloric acid (37%), ethanol (99%), sodium nitrate (99%), commercial Evonik P25-TiO_2 powder, and risperidone (98%) were provided from Sigma–Aldrich Chemie (Steinheim, Germany). Natural graphite (99.99% purity, 20 μm, from Sigma–Aldrich Chemie) was used as precursor of graphene oxide (GO). Acetonitrile, LC/MS water and formic acid were obtained from Merck (Darmstadt, Germany). HPLC grade water was from MilliQ System Academic (Waters, Millipore). HPLC grade methanol (BDH) and acetonitrile (Aldrich) were filtered through a 0.45 μm filter before use. Reagent grade formic acid was from Fluka Chemie (Sigma).

2.2. Synthesis of graphene oxide

GO was prepared from graphite powder according to the modified method reported by Hummers and Offeman [27,28]. Briefly, 1.0 g of graphite and 0.5 g $NaNO_3$ were added into 23 mL of 273 K concentrated H_2SO_4. Next, 3 g of $KMnO_4$ was added gradually with continuous stirring and cooling, while at the same time the temperature of the mixture was maintained below 293 K. Then, the ice-bath was removed and the obtained mixture was stirred at 308 K for 30 min. After that time, 46 mL of distilled water was added

slowly in order to reach temperature of 371 K, and at that temperature the mixture was maintained for 15 min. The resultant reaction was terminated by addition of 140 mL of distilled water followed by 10 mL of 30% H_2O_2 aqueous solution. The GO was collected by centrifugation. The solid materials were washed repeatedly with water and ethanol. The resultant materials were dried under vacuum overnight at 323 K to obtain GO.

2.3. Preparation of reduced graphene oxide—TiO_2 composites (hydrothermal method)

GO was first dissolved in H_2O by ultrasonic treatment for 1 h to yield a yellow-brown solution. TiO_2–P25 was added into the GO colloidal solution and the mixture was stirred for another 1 h. The homogeneous suspension was transferred to a Teflon-lined autoclave and was subjected to hydrothermal treatment at 453 K for 6 h [27,29,30]. It has been reported [29,30] that besides temperature the autogenous pressure developed inside the sealed autoclave also contributes to the reduction of GO. TiO_2–rGO nanocomposites were synthesized with a weight ratio between rGO and TiO_2–P25 at 1:5 (denoted as TiO_2–rGO_{20}) and 1:10 (denoted as TiO_2–rGO_{10}). The obtained composites was collected by centrifugation, washed repeatedly with water, and dried under vacuum at 333 K.

2.4. Materials characterization

Characterizations of the synthesized TiO_2rGO materials were performed, including SEM, TEM,XRD, FT-IR, UV–vis spectroscopy and calculation of the surface area.

The morphology of the materials was studied by scanning electron microscopy (SEM) using a JOEL microscope (JSM-5600, JEOL, Tokyo, Japan) while transmission electron micrographs were obtained using a JEOL JEM-2010F microscope (TEM).

In addition, the crystal structures of materials were investigated by X-ray diffraction (XRD), using a D8 Advance Brüker diffractometer operating with Cu Kα radiation ($\lambda = 0.154$ nm) and a secondary beam graphite monochromator. Powder samples were scanned over an angular 2θ range from 5 to 90°.

Fourier Transform Infrared spectra (FTIR) were acquired using a Perkin Elmer (spectrum 100, Waltham, MA, USA) Infrared spectrophotometer.

UV–vis absorption spectra were obtained using a Jasco V-570 UV–vis spectrophotometer (Hachioji, Japan).

The specific surface area, of the synthesized photocatalysts was calculated from N_2 adsorption–desorption isotherms obtained with a Quandachrome gas adsorption instrument (QUANDACHROM, Bounton Beach, FL, USA).

2.5. Irradiation experiments

Photocatalytic activities of the catalysts (TiO_2–P25, TiO_2–rGO_{20}, TiO_2–rGO_{10}) were assessed through the photodegradation of risperidone (RS) under a variety of experimental conditions, such as, different aqueous matrices (distilled, tap, river and lake water) under artificial solar light and visible light. The catalysts (5 mg) were suspended in an aqueous solution of RS (2 mg L^{-1}, 50 mL) with a magnetic stirring bar in a cylindrical quartz glass reactor that was positioned at 18 cm distance from light source. Catalyst loadings were relatively low (100 mg L^{-1}) in order to obtain slower kinetics and compare the performance of the respectively materials, as well as to avoid dark zones in the illuminated slurry. Irradiation was carried out using a Suntest CPS+ apparatus from Heraeus (Hanau, Germany) equipped with a Xenon arc lamp (1500 W) and glass filters restricting the transmission of wavelengths below 290 nm (simulated solar light). For visible light experiments a cutoff long pass filter was used ($\lambda > 430$ nm). Chamber temperature

was regulated by pressurized air cooling circuit and monitored using thermocouples supplied by the manufacturer. The temperature of samples did not exceed 20 °C using tap water cooling circuit for the reactor. Before irradiation, the suspensions were allowed to stay in the dark for 60 min under stirring, during which the solution concentration was monitored and adsorption equilibrium on the surface of the catalysts was reached. In all cases, to remove catalyst particles the solution samples were passed through 0.45 μm filters and were further analyzed with the appropriate analytical technique. Direct photolysis in the absence of catalyst was also performed as blank experiment in order to calculate its contribution in the degradation of the pollutant.

The experiments revealed that the photocatalytic degradation of RS can be ascribed to a pseudo-first order kinetic model, as described by the following equation:

$$C = C_0 e^{-kt} \tag{1}$$

where C corresponds to pollutant concentration, k is the pseudo-first order kinetic constant, t is the reaction time and C_0 is RS concentration for $t = 0$ (after adsorption equilibrium is reached). The values of k were obtained by non-linear regression or a linear regression on a $logC$ vs t plot.

The irradiation experiments on intermediates were carried out in Pyrex glass cells, filled with 5 mL of a suspension containing the drug (10 mg/L) and the catalyst (500 mg/L). Samples were subjected to different irradiation times (ranging from 5 min to 24 h), using a Philips TLK/05 lamp 40 w with maximum emission at 360 nm. The temperature reached during irradiation was 26 °C.

2.6. Analytical procedures

2.6.1. Liquid – Chromatography – MS

The analysis was carried out using liquid chromatography (LC–MS Shimadzu, Japan), equipped with an auto sampler (SIL-20A, Shimadzu, Japan) and a mass spectrometry detector (LC–MS 2010- EV, Shimadzu, Japan). The analytical column was a Pinnacle II C18 (150 × 4.6 mm, 5 μm Restek, Bellefonte, PA). The mobile phase consisted of acetonitrile and 0.1% formic acid in LC/MS water. Gradient elution was performed using 100/0–0/100 water/acetonitrile in 20 min and 0/100 for further 5 min. The column was equilibrated for an additional 5 min before the next sample injection. Flow rate was 1 mL min^{-1} and the volume injected was 20 μL. Chromatographic separation was carried out using ESI negative mode at 40 °C. The nebulizer pressure was 75 bar (1125 psi) and the detector voltage (V) 1500.

The identification of intermediate products was performed by HPLC/HRMS. The chromatographic separations, monitored using an MS analyzer, were run on a Phenomenex Luna C18 (2) 150 × 2.1 mm × 3 μm particle size, using an Ultimate 3000HPLC instrument (Dionex, Thermo Scientific, Milan, Italy). Injection volume was 20 μL and flow rate was adjusted at 200 μL min^{-1}. Gradient mobile phase composition was adopted: 5/95–100/0 in 40 min methanol/formic acid 0.05% v/v in water when run on ESI positive mode or acetonitrile/ammonium acetate 0.1 mM in the negative mode.

A LTQ Orbitrap mass spectrometer (Thermo Scientific, Milan, Italy) equipped with an atmospheric pressure interface and an ESI ion source was used. The LC column effluent was delivered into the ion source using nitrogen as both sheath and auxiliary gas. The tuning parameters adopted for the ESI source were: capillary voltage 37.00 V, tube lens 65 V. The source voltage was set to 3.5 kV. The heated capillary temperature was maintained at 275 °C. The acquisition method used was optimized before and in the tuning sections for the parent compound (capillary, magnetic lenses and collimating octapole voltages) to achieve maximum sensitivity.

Mass accuracy of recorded ions (vs calculated) was ± 10 millimass units (mmu) (without internal calibration).

Analyses were run using full MS (50–1000 m/z range), MS^2 and MS^3 acquisition in the positive ion mode, with a resolution of 30,000 in FTMS mode. The ions submitted to MS^n acquisition were chosen on the base of full MS spectra abundance without using automatic dependent scan. Collision energy was set to 30 (arbitrary units) for all of the MS^n acquisition methods. MS^n acquisition range was between the values of ion trap cut-off and m/z of the fragmented ion. Xcalibur (Thermo Scientific, Milan, Italy) software was used both for acquisition and for elaboration.

2.6.2. Ion chromatography

A Dionex instrument was employed equipped with a conductometer detector. The determination of ammonium ions was performed by adopting a CS12A column and 25 mM methanesulphonic acid as eluent, at a flow rate of 1 mL min^{-1}. In such conditions, the retention time of ammonium was 4.7 min. The anions were analysed by using an AS9HC anionic column and a mobile phase composed of NaHCO$_3$ 12 mM and K$_2$CO$_3$ 5 mM at a flow rate of 1 mL min^{-1}. In these experimental conditions the retention times of fluoride, nitrite and nitrate were 4.70, 8.30 and 9.58 min, respectively.

2.6.3. Total organic carbon analyzer

Total organic carbon (TOC) was measured on filtered suspensions using a Shimadzu TOC-5000 analyzer (catalytic oxidation on Pt at 680 °C). The calibration was performed using standards of potassium phthalate.

2.7. Toxicity measurements

The toxicity of samples collected at different irradiation times was evaluated with a Microtox Model 500 Toxicity Analyzer (Milan, Italy). Acute toxicity was evaluated with a bioluminescence inhibition assay using the marine bacterium *Vibrio fischeri* by monitoring changes in the natural emission of the luminescent bacteria when challenged with toxic compounds. Freeze-dried bacteria, reconstitution solution, diluent (2% NaCl) and an adjustment solution (non-toxic 22% sodium chloride) were obtained from Azur (Milan, Italy). Samples were tested in a medium containing 2% sodium chloride, in five dilutions, and luminescence was recorded after 5, 15 and 30 min of incubation at 15 °C. Since no substantial differences were found between the three contact times, hereafter the results related to 5 min of contact are reported. Inhibition of luminescence, compared with a toxic-free control to give the percentage inhibition, was calculated following the established protocol using the Microtox calculation program.

3. Results and discussion

3.1. Materials characterization

3.1.1. Scanning and transmission electron microscopy (SEM, TEM)

Fig. S1 shows a SEM image of TiO$_2$–rGO$_{10}$ and TiO$_2$–rGO$_{20}$ composites to illustrate their morphological information. TiO$_2$–rGO$_{20}$ composite shows the dispersed TiO$_2$ particles on graphene sheets without much aggregation. According to TEM images (Fig. S2), the obtained composites retained the two-dimensional transparent sheet structure with wrinkles, while P25 nanoparticles with the size of 20–30 nm were dispersed on graphene sheets. Our findings are in agreement with previous observations [27] showing that the increase in rGO content in the hydrothermal composites increases the dispersion of titania nanoparticles on the graphene sheets.

3.1.2. X-ray diffraction (XRD)

The X-ray diffraction was employed to characterize the crystal structure of the synthesized GO, as well as, the TiO$_2$–rGOcomposites (Fig. S3). The XRD pattern of GO showed a strong and sharp diffraction peak at 2θ of 10.90°. This illustrates that most of the natural graphite was oxidized into GO. When hydrothermal reduction was employed for the preparation TiO$_2$–rGO this diffraction peak disappeared and a XRD pattern similar to the composition of TiO$_2$ was obtained. This observation could be attributed the reduction of GO to graphene sheets and the effective intercalation of TiO$_2$ to produce the final composite. The TiO$_2$–rGO composites prepared by the other methods showed similar XRD [27].

3.1.3. FT-IR patterns

Fig. S4 shows FT-IR patterns of GO and TiO$_2$–rGO$_{20}$ composite. It is clear that the GO shows many strong absorption peaks. A broad IR peak around 3486 cm^{-1} can be identified, corresponding to the O—H stretching vibration, at 1720 cm^{-1} which is attributed to the C=O stretching vibration of carboxylates/ketones groups, C=C stretching at around 1624 cm^{-1}, alcoholic C—OH bending at 1418 cm^{-1}, at 1224 cm^{-1} due to C—O stretching modes in epoxy group and C—O stretching at 1057 cm^{-1} [31]. These characteristic absorption bands decreased drastically in intensity or even disappeared in the case of the TiO$_2$–rGO composites indicating a significant reduction of GO. Typically Ti—O—Ti and Ti—O—C bonds show low frequency bands around 500–700 cm^{-1} [27]. Therefore, the broad band at the low frequency region in the TiO$_2$–rGO$_{20}$ composite can be considered combination of Ti—O—Ti and Ti—O—C vibrations because of the chemical interaction of TiO$_2$ particles with the rGO. The above results further confirmed the reduction of GO and the successful preparation of chemical-coupling TiO$_2$–rGO composites.

3.1.4. BET isotherm

Regarding the textural characterization, Fig. S5 shows the N$_2$ adsorption–desorption isotherm. Isotherm showed an adsorptive behavior of type-II, in accordance with IUPAC classification, characteristic of macro porous materials or of materials presenting low porosity [30,31]. The total specific surface area of TiO$_2$–rGO$_{20}$ was found to be 84 m^2 g^{-1} using a BET plot. The specific area of the TiO$_2$–rGO$_{10}$ was measured at 68 m^2 g^{-1} and TiO$_2$–P25 at 52 m^2 g^{-1}.

3.1.5. UV–vis spectra

The visible light responsive properties of pure TiO$_2$–P25 and TiO$_2$–rGO composites with different rGO content are expressed by UV–vis absorption spectra. Compared with the TiO$_2$–P25 nanoparticles, the prepared TiO$_2$–rGO composites depict an improved UV light absorption (Fig. S6). A red shift of the absorption edge of TiO$_2$ upon the addition of rGO, is observed and it is attributed to the formation of Ti—O—C bonds between the interface of TiO$_2$ and rGO [32–34]. With increasing amount of the rGO, the TiO$_2$–rGO composites show enhanced visible-light absorption. To be more specific, the band gaps determined were 3.0 and 2.7 eV for TiO$_2$–rGO$_{10}$ and TiO$_2$–rGO$_{20}$, respectively; lower than that of TiO$_2$–P25 (3.3 eV) showing that the degree of band gap narrowing increases with the content of RGO in the composite.

3.2. Adsorption in dark phase and photolysis

Preliminary experiments under dark conditions were performed to establish the adsorption–desorption equilibrium of RS in aqueous solutions (pH levels: 3.5, 7.0 and 10.5) with TiO$_2$–P25 and TiO$_2$–rGO composites. The highest adsorption capacity (60%) was obtained at pH 7.0 withTiO$_2$–rGO$_{20}$catalyst.The RS molecules are mainly protonated in this pH solution, while the surface charge

of the composite material is negatively charged (pH PZC $\approx$ 3.2) and electrostatic attractions are expected between them. In the case of pH 3 and TiO$_2$–P25, electrostatic repulsions take place between protonated RS molecules and titania surface (pH PZC $\approx$ 6.8) due to the positively charged catalyst surface and therefore adsorption efficiency is the lowest (<12%). Moreover, the surface area of the catalysts could also affect the different adsorption capacities since in all cases, irrespectively of pH level, adsorption was higher in the composite TiO$_2$–rGO$_{20}$ (S$_{BET}$ 84 m^2 g^{-1}) material compared to TiO$_2$–P25 (S$_{BET}$ 52 m^2 g^{-1}).

Hydrolysis as well as direct photolysis (2 h) showed that these processes were unable to degrade RS in the absence of the catalyst.

3.3. Photocatalytic performance

The photocatalytic activity of TiO$_2$–P25 catalyst and TiO$_2$ based composite materials with different rGO contents was evaluated under artificial solar light and visible light in distilled water, as well as, different surface waters (at natural pH) with respect to RS degradation. The corresponding pseudo-first order rate constants (k), as well as the half-lives ($t_{1/2}$) are reported in Table 1.

Fig. 1 depicts the photocatalytic performances of the benchmark TiO$_2$–P25 titania catalyst, TiO$_2$–rGO$_{10}$ and TiO$_2$–rGO$_{20}$ composites in degradation of RS under simulated solar light and different aqueous matrices.

The photodegradation of RS over titania P25 catalyst and composites of TiO$_2$–P25 with different rGO contents under simulated solar irradiation showed that the efficiency decreases in the order: distilled water > tap water > river water > lake water, showing a strong dependence on the constitution of the irradiated media (Fig. 2a). This may be attributed to the increased organic carbon content (lake water, 13.0 mg L^{-1}, river water 2.7 mg L^{-1}, tap water 0.5 mg L^{-1}, distilled water 0.0 mg L^{-1}, included in Table 1), which is expected to decrease RS conversion, but also to the presence of various species (e.g. Cl$^-$, HCO$_3^-$, CO$_3^{2-}$) and other reactive moieties competing for OH$^\bullet$ radicals (scavengers) and photocatalyst surface sites.

The commercial TiO$_2$–P25 shows a high photocatalytic activity for the decomposition of RS in all aqueous matrices owing to its well-known performance for various photocatalytic reactions. The presence of rGO nanosheets (10%) in TiO$_2$–P25 shows that the resultant P25–rGO$_{10}$ composite depicts an enhanced photocatalytic activity in the investigated aqueous media compared to titania. A further increase of the rGO content at 20% resulted in a remarkably increment of the photocatalytic activity of the respective P25–rGO$_{20}$ composite (Fig. 2a).
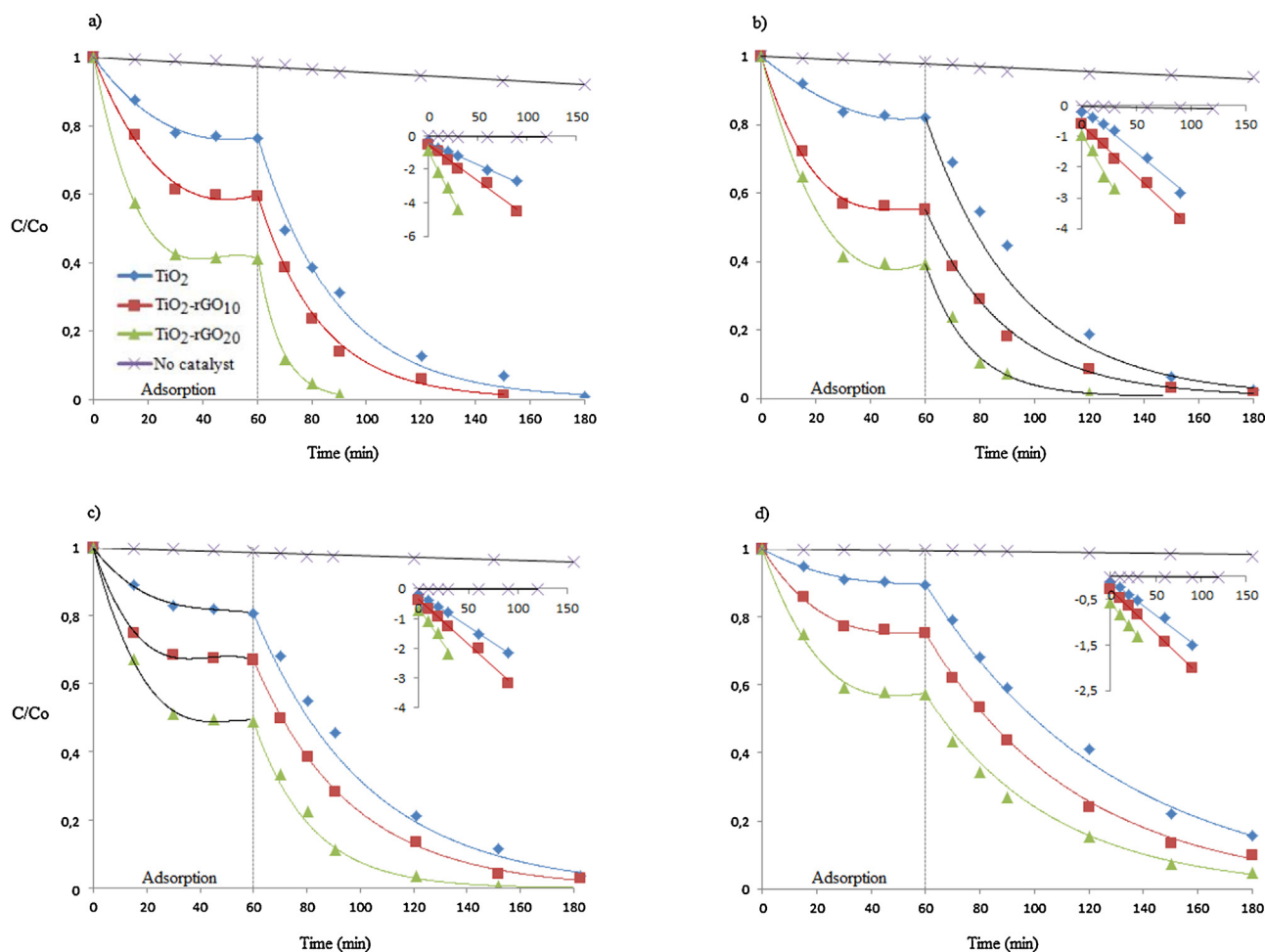
Irrespectively of the irradiated aqueous matrix, the photocatalytic efficiency of the tested materials for RS degradation under simulated solar light follows the order: TiO$_2$–rGO$_{20}$ > TiO$_2$–rGO$_{10}$ > TiO$_2$–P25. In other words, the increasing amount of graphene oxide in the hybrid composites leads to higher pseudo-first order rate constants for RS degradation (18 × 10^{-3} and 21 × 10^{-3} min^{-1}, in lake water, Table 1) than that observed for the bare TiO$_2$–P25 material (15 × 10^{-3} min^{-1}).

The observed enhancement of the photocatalytic activity is reported as due to the inhibition of electron-hole recombination [34–36]. The enhanced photocatalytic activity in the TiO$_2$–rGO composites could be also associated to the surface area and the adsorption capacity of these materials, since the increasing amount of rGO to P25 titania resulted in a higher adsorption ability of RS. The adsorption and kinetic analyses of the results obtained with the composite materials will be discussed in the framework of a two-phase model in a forthcoming paper (part II of this study).

A decrease of the photocatalytic activity of TiO$_2$–rGO composites at a rGO content >5% wt has been reported during methylene blue photocatalytic degradation [32]; however, this was not observed in

Table 1
The corresponding pseudo-first order rate constants (k), as well as, the half-lives ($t_{1/2}$) of RS photocatalytic degradation.

	Simulated solar irradiation			Visible light		
	TiO$_2$ $k \times 10^{-3}$ (min^{-1})	TiO$_2$–rGO$_{10}$	TiO$_2$–rGO$_{20}$	TiO$_2$ $k \times 10^{-3}$ (min^{-1})	TiO$_2$–rGO$_{10}$	TiO$_2$–rGO$_{20}$
Distilled	26.4	42.6	115.5	6.98	22.8	69.8
Tap	29.3	33.6	61.6	5.35	9.54	30.6
River	22.2	30.3	48.4	4.01	8.09	24.4
Lake	15.1	19.2	24.8	1.42	6.10	10.4

Fig. 1. Photocatalytic oxidation of RS at various irradiated media under simulated solar irradiation. (a) distilled water, (b) tap water, (c) river water and (d) lake water. The inset represents the linear plots of pseudo-first order equation (lnC=lnCo –kt) of the respective curves.

our study. The decreased efficiency observed was ascribed to the increase in the opacity and light scattering of TiO$_2$–rGO composite, and high graphene load shielding the TiO$_2$ from absorbing UV light, resulting in rapid decrease of irradiation passing through the reaction suspension solution [33,37].

Meanwhile, we also evaluated the photocatalytic photodegradation of RS aqueous solutions under visible light. The corresponding results are presented in Fig. 2b and Table 1, respectively. The performance of the catalysts under visible light irradiation follows the same order: TiO$_2$–rGO$_{20}$ > TiO$_2$–rGO$_{10}$ > TiO$_2$–P25 in all cases. The composites prepared with rGO content of 20 wt% (TiO$_2$–rGO$_{20}$) exhibited the larger photocatalytic efficiency. Compared with the simulated solar irradiation the respective pseudo-first order rate constants under visible light irradiation were lower. This behavior was expected since the same light source (lamp) was used in both cases and the selected cut-off filter permits only irradiation with λ > 430 nm.

What was more important to notice was the fact that photocatalytic degradation efficiency for the composite materials was significantly higher compared to TiO$_2$–P25 under visible light irradiation. A similar behavior has been reported recently [35,38–40], that corroborate the role of rGO in extending the photocatalytic activity of TiO$_2$ under visible light illumination. The higher photocatalytic degradation rates of TiO$_2$–rGO composites under visible light illumination can be attributed to the active role of the carbon phase acting as sensitizer as it is discussed elsewhere (part II of this study).

The most active photocatalyst (TiO$_2$–rGO$_{20}$) was also tested to evaluate its stability in successive photocatalytic reactions for RS degradation under simulated solar irradiation in tap water. After each photocatalytic experiment the catalyst was washed with distilled water and dried in the oven at 100 °C for 3 h before re-used. As presented in Fig. 2c, the TiO$_2$–rGO$_{20}$ photocatalyst after being used for five consecutive times, preserved its activity (88%), indicating
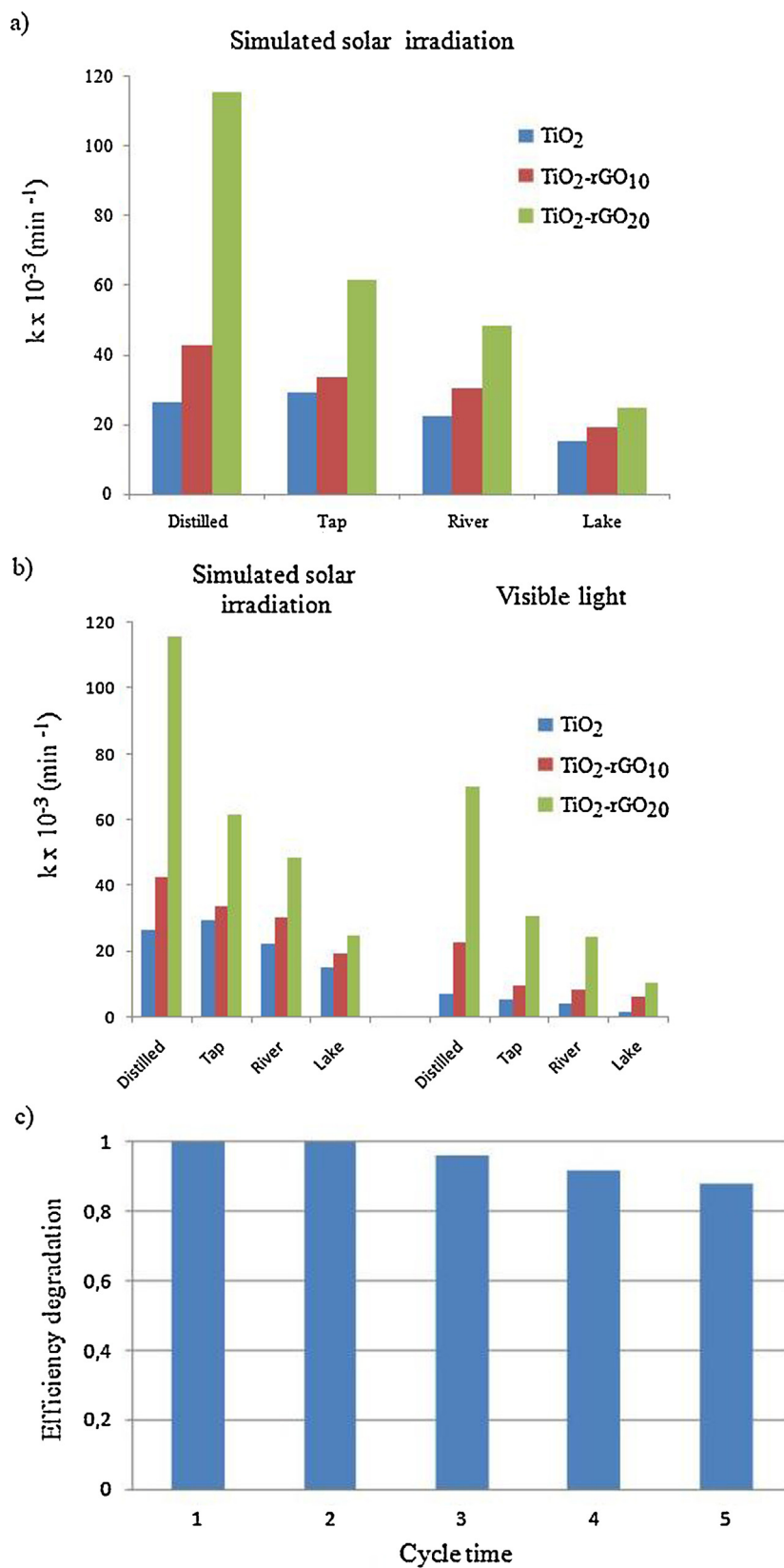
Fig. 2. (a) Rate constants (k) of risperidone decomposition by various photocatalysts under simulated solar irradiation; (b) rate constants (k) of risperidone decomposition by various photocatalysts under visible light, (c) the repeated photocatalytic performance of TiO_2–rGO_{20} under simulated solar irradiation.
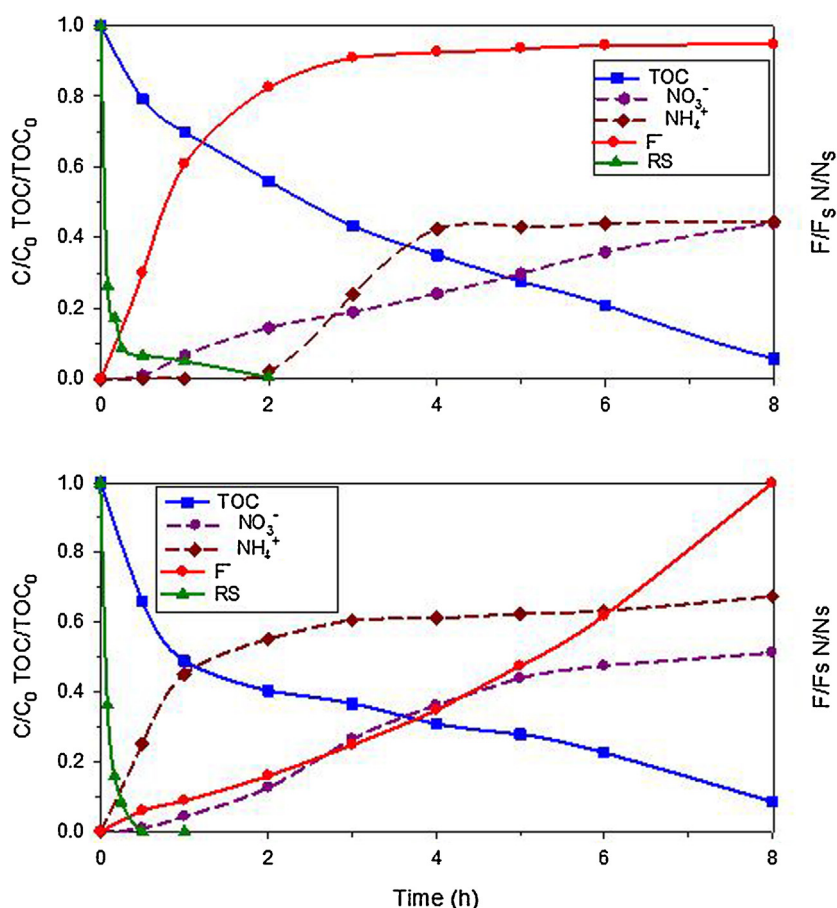
Fig. 3. Risperidone disappearance, TOC profile and evolution of inorganic ions as a function of irradiation time; (top) in the presence of TiO_2–P25 and (bottom) in the presence of TiO_2–rGO_{10}.

catalyst stability and showing a good potential in photocatalysis applications.

3.4. Risperidone degradation products under heterogeneous photocatalysis

Risperidone (RS) was irradiated under UV–A in the presence of bare titanium dioxide (TiO_2–P25) or composite material (TiO_2–rGO_{10}) and analyses were run in the ESI positive mode, which appeared to be more sensitive and suitable both for the parent compound and for most of the photogenerated products. The addition of the photocatalyst endorsed a fast degradation and RS ($[M+H]^+$ 411.2335) was efficiently degraded ($t_{1/2}$ 10 and 5 min with TiO_2–P25 and TiO_2–rGO_{10}, respectively, Fig. 3). A complete disappearance of RS was observed within 60 (TiO_2–P25) or 30 (TiO_2–rGO_{10}) min of irradiation. Along with RS decomposition, in the presence of TiO_2–P25 the formation of twenty intermediate compounds (TPs) occurred, and their evolution profiles are plotted in Fig. S7. When using the hybrid material, even more TPs (34) were detected, whose profiles are plotted in Fig. S8. Even if the same kind of TPs is formed in the two cases, the employment of composite material leads to the formation of an higher number of isobaric species. Furthermore, the relative TPs abundance in the two cases is different. These differences could be attributed to the occurrence of a diverse mechanism with the two materials, as two phases are involved (TiO_2 and rGO).

These TPs are formed in the initial steps of the photocatalytic treatment and their highest level was observed when more than a half of the RS was transformed. Considering the TiO_2–rGO_{10} composite, most TPs were quickly degraded within 30 min of irradiation, while with TiO_2–P25 2 h of irradiation are required to completely abate them; it has to be noted that four of them are still present after 4 h of irradiation.

These derivatives are collected in Table 2 and can be grouped into three classes: TPs resulting from (poli) hydroxylation and/or demethylation of the molecule (from **I** to **V**), those involving defluorination (**XII**) and those resulting from the molecule breakage (from **VI** to **XI** and from **XIII** to **XVI**). The positive-ion ESI mass spectra of RS transformation products provided a useful means for the determination of the molecular mass. High resolving power was useful to attribute their empirical formula; accurate *m/z* values of parent ions were reported with error below 1 mmu, which guarantee the correct assignment of their molecular formula in all cases, while their MS^2 and MS^3 spectra showed several structural-diagnostic ions that allowed to characterize the different TPs and to distinguish the isobaric species (see Table S1). The proposed structures are consistent with the fragmentation profiles of their protonated forms, as shown in supplementary information for all intermediate products (see Schemes S2–S10).

RS MS^n study allowed obtaining information useful to identify unknown transformation products formed through drug degradation. The product ions generated from protonated molecular ions of risperidone are collected in Table S1 and Scheme S1. MS^2 spectrum shows the product ion at 191.1249 *m/z*, due to the molecule breakage. In MS^3 risperidone spectrum, two product ions were detected at 110.0632 and 163.1283 *m/z*, due to the cleavage of the pyrimidine ring and the loss of CO; these routes have been carefully considered in the structure attribution of unknown compounds presented below.

Table 2
List of $[M+H]^+$ obtained from RS and its intermediate compounds showed in Figs. S6 and S7

$[M+H]^+$ (empirical formula)	Name	t_R (min)	$[M+H]^+$ (empirical formula)	Name	t_R (min)
411.2335 ($C_{23}H_{28}FN_4O_2$)	RS	9.35	461.2255 ($C_{23}H_{30}FN_4O_5$)	V-B	9.16
427.2193 ($C_{23}H_{28}N_4O_3$)	I-A	8.55	461.2255 ($C_{23}H_{30}FN_4O_5$)	V-C	9.73
427.2193 ($C_{23}H_{28}N_4O_3$)	I-B	9.16	461.2255 ($C_{23}H_{30}FN_4O_5$)	V-D	10.37
427.2193 ($C_{23}H_{28}N_4O_3$)	I-C	11.36	301.2069 ($C_{17}H_{25}N_4O$)	VI	3.55
443.2011 ($C_{23}H_{28}FN_4O_4$)	II-A	6.35	221.1119 ($C_{12}H_{14}FN_2O$)	VII	7.54
443.2011 ($C_{23}H_{28}FN_4O_4$)	II-B	8.32	183.1155 ($C_8H_{11}N_2O_3$)	VIII	1.93
443.2011 ($C_{23}H_{28}FN_4O_4$)	II-C	8.72	111.0929 ($C_6H_{11}N_2$)	IX	2.67
443.2011 ($C_{23}H_{28}FN_4O_4$)	II-D	9.01	141.1041 ($C_7H_{13}ON_2$)	X	1.79
443.2011 ($C_{23}H_{28}FN_4O_4$)	II-E	10.17	99.0926 ($C_5H_{11}N_2$)	XI	1.78
459.1960 ($C_{23}H_{28}FN_4O_5$)	III-A	5.91	409.2279 ($C_{23}H_{29}N_4O_3$)	XII-A	7.02
459.1960 ($C_{23}H_{28}FN_4O_5$)	III-B	7.88	409.2279 ($C_{23}H_{29}N_4O_3$)	XII-B	7.77
459.1960 ($C_{23}H_{28}FN_4O_5$)	III-C	8.72	409.2279 ($C_{23}H_{29}N_4O_3$)	XII-C	9.16
459.1960 ($C_{23}H_{28}FN_4O_5$)	III-D	9.59	409.2279 ($C_{23}H_{29}N_4O_3$)	XII-D	9.88
459.1960 ($C_{23}H_{28}FN_4O_5$)	III-E	10.03	321.1636 ($C_{17}H_{22}FN_2O_3$)	XIII	8.02
475.2239 ($C_{23}H_{28}FN_4O_6$)	IV-A	4.59	319.1477 ($C_{17}H_{20}FN_2O_3$)	XIV	8.47
475.2239 ($C_{23}H_{28}FN_4O_6$)	IV-B	5.77	337.1588 ($C_{17}H_{22}FN_2O_4$)	XV	8.50
475.2239 ($C_{23}H_{28}FN_4O_6$)	IV-C	8.13	293.1322 ($C_{15}H_{18}FN_2O$)	XVI	8.72
461.2255 ($C_{23}H_{30}FN_4O_5$)	V-A	6.40			

3.4.1. Characterization of TPs formed during the irradiation

Three species with 427.2193 m/z and empirical formula $C_{23}H_{28}N_4O_3F$ were formed with TiO_2–rGO_{10} (named **I-A** to **I-C**) and attributed to monohydroxylated risperidone, while with TiO_2–P25 a single species was identified (**I-A**). Considering **I-A**, MS^2 spectrum exhibited two key product ions at 191.1239 and 207.1194 m/z, both attributable to the detachment of hydroxylated pyrimidine moiety. MS^3 analysis on the precursor ion 207.1194 m/z showed the formation of the product ions at 163.0865 and 189.1022 m/z, involving the loss of a molecule of acetaldehyde or water, respectively, allowing the location of the OH group on the 9 position. All these ions could be linked together as shown in Scheme S2. It has to be underlined that this compound matched with the main human metabolite formed from RS [41]. For the other two isomers the involvement of OH substitution close to ethylene central bridge was critical (Scheme S2). 177.1011 m/z ion formed from **I-B** was explainable by a retro–Diels–Alder reaction, consequently **I-B** can be described as the isomer hydroxylated on the ethylene bridge.

Five species with $[M+H]^+$ 443.2011 and empirical formula $C_{23}H_{28}FN_4O_4$ attributable to dihydroxyl-derivatives were detected with TiO_2–rGO_{10} and only two with TiO_2 (named **II-A** and **II-B**). **II-A** exhibited three structural diagnostic ions at 205.037, 223.1149 and 233.1160 m/z, due to the formation of monohydroxyled, dihydroxylated pyrimidine ions or to the detachment of the pyrimidine moiety, respectively (Scheme S3, top), permitting the location of both OH groups on the pyrimidine moiety. Analyzing **II-B**, the contemporaneous formation of the product ions 207.11494 and 233.1160 m/z suggested the presence of one (of the two) OH groups on the ethylene bridge. Isomers **II-C** to **II-E** cannot be further characterized.

Five (or two) species at 459.1960 m/z and three (or one) species at 475.2239 m/z were formed with TiO_2–rGO_{10} or TiO_2–P25 and attributed to trihydroxylated and tetrahydroxylated derivative (named **III-A** to **III-E** and **IV-A** to **IV-C**).

Key product ions formation permitted to locate in **III-A** and **IV-A** all the OH groups on the fluorobenzo[*d*]isoxazol moiety, and in **III-B** and **IV-C** all OH groups on the pyrimidine moiety (Schemes S4 and S5).

Four (or three) isobaric species at 461.2255 m/z were detected with TiO_2–rGO_{10} or TiO_2–P25 and attributed to the trihydroxylation/reduction of the molecule (named **V-A**, **B**, **C** and **D**).

MS^2 spectrum for TP **V-A** showed two prominent ions, 191.1219 and 441.2174 m/z, attributed to the detachment of the unmodified pyrimidine moiety and loss of a molecule of HF. Therefore, two OH groups could be tentatively located on the piperidine and an OH group on the pyrimidine ring (Scheme S6).

V-B, C and **D** MS^2 spectra exhibited the formation of the ions 233.1127 and 443.2101 m/z, formed through the elimination of the unmodified fluorobenzo[*d*]isoxazol moiety and the loss of a water molecule. Unfortunately, the information was not enough to attribute the exact position for hydroxylation.

Four compounds at m/z 409.2279, attributed to the defluorinated and monohydroxylated derivatives were formed with TiO_2–rGO_{10} (**XII-A** to **XII-D**), while only one species (**XII-B**) was detected with TiO_2–P25. The formation of the product ion at 191.1219 m/z in MS^2 spectrum of **XII-B** and **XII-C** permitted to exclude the hydroxylation on the pyrimidine moiety. Conversely, in **XII-D** MS^2 spectrum, the formation of product ion at 189.1023 m/z allowed to locate the OH group in the pyrimidine substructure (Scheme S7).

Ten species with lower carbon content were formed through the cleavage of the drug molecule with both catalysts. A transformation product at 301.2069 m/z (named **VI**) was detected with both catalysts and formed through the detachment of fluorophenol. MS^2 and MS^3 spectra showed as prominent ions the same ions already detected in risperidone MS^n spectra, all involving the pyrimidine/piperazine moiety. The proposed fragmentation pathway is depicted in Scheme S8.

Four species were formed though the cleavage of the pyrimidine moiety: the monohydroxylated compound at 321.1636 m/z (named **XIII**), further transformed into the keto derivative (319.1477 m/z, named **XIV**) or the bihydroxylated derivative (337.1588 m/z, named **XV**), further subjected to dealkylation (293.1322 m/z, named **XVI**).

An additional transformation pathway involved the drug cleavage with the formation of the ion 221.1119 m/z, (named **VII**) with empirical formula $C_{12}H_{13}N_2OF$, well matched with the detachment of the pyrimidine moiety. MS^2 and MS^3 spectra confirmed this structure (Scheme S9).

At longer irradiation time some additional transformation products were detected at 183.1155 (named **VIII**) and 111.0929, 141.1041 and 99.0926 m/z (named **IX, X** and **XI**); their empirical formulas allowed to assign respectively the following structures: dihydroxy -tetrahydro-4H-pyrido[1,2-a]pyrimidin-4-one, 4-cyano-N-methylpiperidine, 2-hydroxy-4-cyano-N-methyl-piperidine and 2-methyl-4-aminobutanonitrile. Fragmentation pathway for the species **X** is reported in Scheme S10.

3.4.2. Overall transformation pathways

Based on the TPs temporal profiles, all the identified compounds formed in the presence of TiO_2–P25 or TiO_2–rGO_{10} could be originated according to eight competitive pathways summarized in Fig. 4. In both cases, the favoured initial transformation routes were
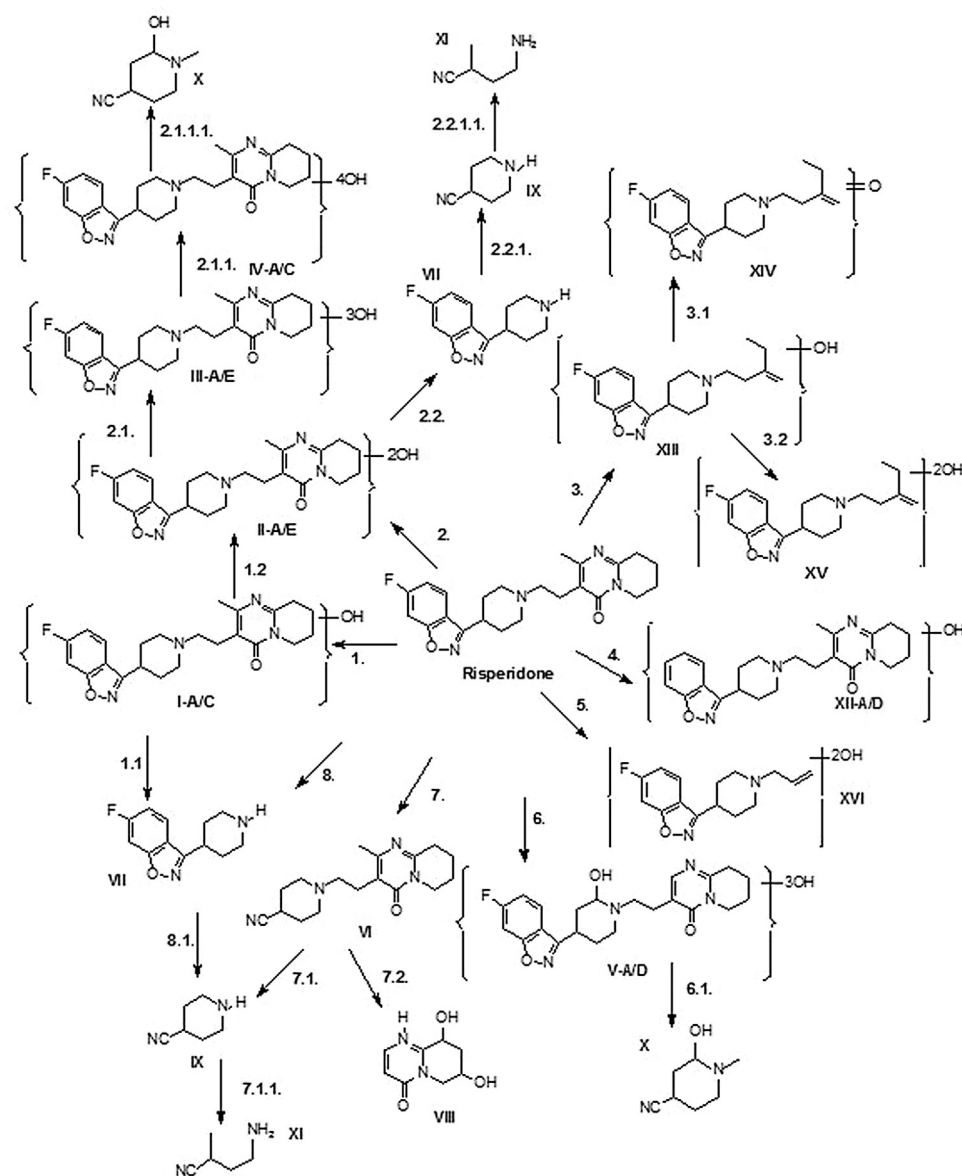
Fig. 4. Proposed transformation pathways followed by risperidone under photocatalytic treatment.

those involving hydroxylation or demethylation processes. Even if both catalysts share the same class of TPs, in the presence of the composite material, these TPs presented additional isomeric forms. This was particularly marked for the transformation routes involving the detachment of fluorine or the cleavage of pyrimidine moiety. Compounds **VIII–XI** are formed at the last stage of RS degradation and **X** and **XI** are not further degraded on TiO$_2$ in the considered time (2 h), while their degradation is complete with TiO$_2$–rGO.

Some of these TPs could also be formed in surface waters, as already recognised to occur with other environmental pollutants [42,43].

3.5. Mineralization process

The TOC profiles evidenced with both materials an initial fast degradation followed by a slower TOC decrease for longer irradiation times; the complete mineralization was only achieved after 16 h of irradiation (Fig. 3). During the first two hours of irradiation the mineralization process quickly proceeded with TiO$_2$–rGO$_{10}$, in

agreement with the fast degradation of all TPs described above (Fig. S7).

By analyzing the fate of inorganic ions, fluorine atom was stoichiometrically recovered as fluoride ions, while the fate of nitrogen was more intriguing. Fluoride ions were easily formed, as fluorine can be easily released from aromatic ring [44], and with TiO$_2$–P25 the stoichiometric concentration was achieved within 4 h of irradiation. Conversely, with TiO$_2$–rGO$_{10}$ defluorination slowly occurred and fluorine was completely released only after 8 h of irradiation.

The transformation of the nitrogen atoms, included in a pyrimidine and piperidine ring, was more complex and slow. In the presence of TiO$_2$–P25, the release of nitrogen started after 30 min of irradiation and it was transformed into ammonium ions and nitrate ions, as shown in Fig. 3. Conversely, in the presence of TiO$_2$–rGO$_{10}$ the molecule cleavage was easily achieved and nitrogen was faster released, mainly in the form of ammonium ions. Pyrimidine moiety yielded predominant formation of ammonium ions [45], while the formation of nitrate ions could be ascribed to the oxazole moiety. After 10 h the nitrogen was recovered in the stoichiometric amount as ammonium (45%) and nitrate (55 %).
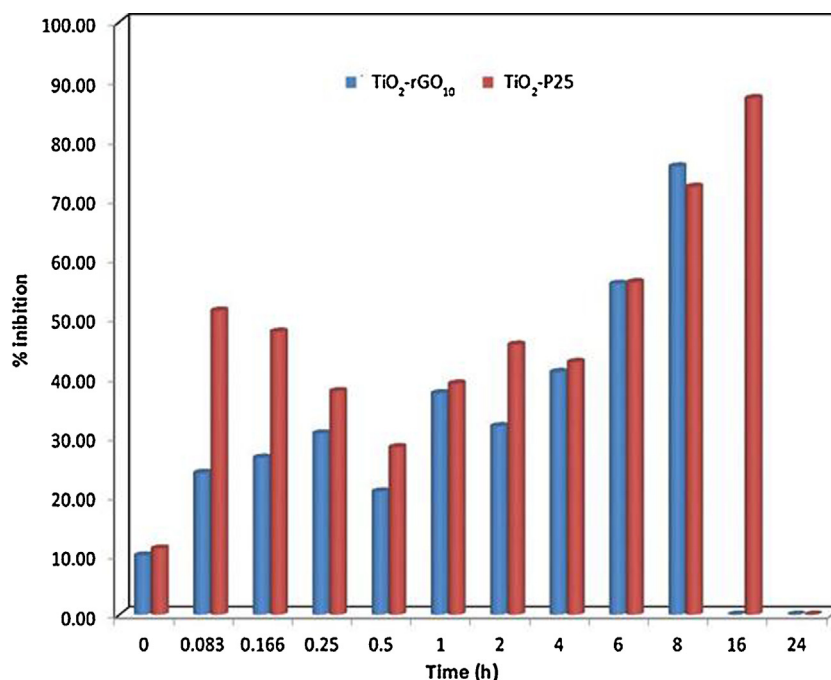
Fig. 5. Acute toxicity of risperidone as a function of irradiation time in the presence of TiO_2–P25 and TiO_2–rGO_{10}.

3.6. Toxicity assessment

Acute toxicity was evaluated by monitoring changes in the natural emission of the luminescent bacteria *Vibrio fischeri* when challenged with toxic compounds and was expressed as percentage of inhibition of the bacteria luminescence. Results obtained on samples subjected to heterogeneous photocatalysis are plotted in Fig. 5.

Acute toxicity increased from 5 min onward. Therefore, while RS is not toxic, its transformation proceeded through the formation of harmful compounds as the percentage of inhibition effect increased as a function of irradiation time. The toxicity profiles were similar with both catalysts, even if in the presence of TiO_2–rGO_{10} the complete abatement of harmful compounds was achieved within 16 h, while at that time with bare TiO_2–P25 a peak in the solutions toxicity was observed and longer time (24 h) were required to abate toxic compounds. This shape suggested the formation of harmful compounds during the different stages of RS transformation; in particular, species formed in the last stages of degradation (e.g. compounds from **VIII** to **XI**) seemed to be more toxic one.

It has to be underlined that the further increase observed at longer irradiation time has to be ascribed to defluorinated compounds, formed through the molecule cleavage; probably, the formation of compounds highly hydrophilic and with very low molecular weight, not detected via LC/MS, occurred.

4. Conclusions

Two hybrid materials, TiO_2–rGO_{10} and TiO_2–rGO_{20} were successfully prepared via a hydrothermal synthesis route and their morphological and textural characteristics, crystal structure as well as optical properties were characterized. TiO_2 particles are well dispersed on rGO sheets in the resulting composites exhibiting improved UV–vis light absorption properties compared to bare TiO_2. The resulting composites were compared in terms of their photocatalytic properties with TiO_2. Results clearly demonstrated the higher photocatalytic activity of the synthesized composites compared to TiO_2-P25, for the transformation of RS. The

photocatalytic activity was more also possible under visible light, at which TiO_2 was almost inefficient. In all cases, the photocatalytic performance decreases in the order distilled water > tap water > river water > lake water, showing a moderate dependence on the composition of the irradiated media.

Numerous unknown transformation products were formed and identified by LC/HRMS, whose formation lead to an increase in acute toxicity. A tentative transformation scheme is proposed and involves eight initial transformation pathways that could match with risperidone environmental behavior.

The present study reveals the effectiveness and benefits of the use of TiO_2-rGO_{10} material, in terms of faster drug disappearance, earlier abatement of toxicity and easier degradation of the transformation products and mineralization.

Appendix A. Supplementary data

Supplementary data associated with this article can be found, in the online version, at http://dx.doi.org/10.1016/j.apcatb.2015.10.010.

References

[1] http://pubchem.ncbi.nlm.nih.gov/summary/summary.cgi?sid=50106975.
[2] http://www.globalpharmaceuticalspk.com/pdf/Peridal%20Leaflet.pdf.
[3] N.M. Weggelaar, W.J. Keijer, P.K.C. Janssen, J. Clin. Psychopharmacol. 31 (2011) 129–131.
[4] V.L. Borova, N.C. Maragou, P. Gago-Ferrero, C. Pistos, N.S. Thomaidis, Anal. BioanalChem. 406 (2014) 4273–4285.
[5] https://sds.edqm.eu/pdf/Pdfs/EDQM_Y0000370_6.0_MSDS_EN.pdf.
[6] N. Ansermot, M. Brawand-Amey, A. Kottelat, C.B. Eap, J. Chromat. A 1292 (2013) 160–172.
[7] R.S. Tomar, T.J. Joseph, A.S.R. Murthy, D.V. Yadav, G. Subbaiah, K.V.S.R. KrishnaReddy, J. Pharmac. Biomed. Anal. 36 (2004) 231–235.
[8] D.S. Fisher, S.J. Partridge, S.A. Handley, L. Couchman, P.E. Morgan, R.J. Flanagan, Forensic. Sci. Internat. 229 (1–3) (2013) 145–150.
[9] P. Calza, V.A. Sakkas, C. Medana, A.D. Vlachou, F. Dal Bello, T.A. Albanis, Appl. Catal. B: Environ. 129 (2013) 71–79.
[10] V.A. Sakkas, P. Calza, A.D. Vlachou, C. Medana, C. Minero, T. Albanis, Appl. Catal. B: Environ. 110 (2011) 238–250.
[11] Y.X. Lin, C. Ferronato, N.S. Deng, J.M. Chovelon, Appl. Catal. B: Environ. 104 (3–4) (2015) 353–360.
[12] D. Kanakaraju, B.D. Glass, M. Oelgemoller, Green Materials for Energy, Products and Depollution, In: E. Lichtfouse, J. Schwarzbauer,D. Robert, eds, Environmental Chemistry for a Sustainable World vol. 3 (2013) 69-133.
[13] J. Rivera-Utrilla, M. Sanchez-Polo, M. Angeles Ferro-Garcia, G. Prados-Joya, R. Ocampo-Perez, Chemosphere 93 (7) (2013) 1268–1287.
[14] A. Fujishima, K. Hashimoto, T. Watanabe, TiO_2 Photocatalysis, Fundamentals and Applications, Bkc Inc., Tokyo, 1999.
[15] I.K. Konstantinou, T.A. Albanis, Appl. Catal. B: Environ. 42 (2003) 319–335.
[16] H.Q. Sun, S.B. Wang, H.M. Ang, M.O. Tade, Q. Li, Chem. Eng. J. 162 (2010) 437–447.
[17] P. Gao, Z. Liu, M. Tai, D.D. Sun, W. Ng, Appl. Catal., B 138–139 (2013) 17–25.
[18] J.H. Byeon, Y.W. Kim, ACS Appl. Mater. Interfaces 5 (2013) 3959–3966.
[19] W. Tu, Y. Zhou, Q. Liu, S. Yan, S. Bao, X. Wang, M. Xiao, Z. Zou, Adv. Funct. Mater. 23 (2013) 1743–1749.
[20] J. Zhang, Z. Zhu, Y. Tang, X. Feng, J. Mater. Chem. A 1 (2013) 3752–3756.
[21] S. Anandan, T. Narasinga Rao, M. Sathish, D. Rangappa, I. Honma, M. Miyauchi, ACS Appl. Mater. Interfaces 5 (2012) 207–212.
[22] A.A. Ismail, R.A. Geioushy, H. Bouzid, S.A. Al-Sayari, A. Al-Hajry, D.W. Bahnemann, Appl. Catal. B Environ. 129 (2013) 62–70.
[23] J. Wang, P. Wang, Y. Cao, J. Chen, W. Li, Y. Shao, Y. Zheng, D. Li, Appl. Catal. B: Environ. 136–137 (2013) 94–102.
[24] P. Wang, J. Wang, X. Wang, H. Yu, J. Yu, M. Lei, Y. Wang, Appl. Catal. B: Environ. 132–133 (2013) 452–459.
[25] Q. Xiang, J. Yu, M. Jaroniec, J. Am. Chem. Soc. 134 (2012) 6575–6578.
[26] X. An, J.C. Yu, F. Wang, C. Li, Y. Li, Appl. Catal. B 129 (2013) 80–88.
[27] W. Fan, Q. Lai, Q. Zhang, Y. Wang, J. Phys. Chem. C 115 (2011) 10694–10701.
[28] W.S. Hummers, R.E. Offeman, J. Am. Chem. Soc. 80 (1958) 1339.
[29] C. Nethravathi, M. Rajamathi, Carbon 46 (2008) 1994–1998.
[30] R.C. Bansal, J.B. Donnet, F. Stoeckli, Active Carbon, Marcel Dekker, New York, 1988.
[31] S. Morales-Torres, L. M. Pastrana-Mart, (nez, J. L. Figueiredo, J. L. Faria, A.M.T. Silva), Applied Surface Science, (2013) 361–368.
[32] P. Wang, J. Wang, X. Wang, H. Yu, J. Yu, M. Lei, Y. Wang, Appl. Catal. B: Environ. 132–133 (2013) 452–459.
[33] Y. Zhang, Z.-R. Tang, X. Fu, Y.-J. Xu, ACS Nano 4 (2010) 7303–7314.
[34] H. Zhang, X. Lv, Y. Li, Y. Wang, J. Li, ACS Nano 4 (2009) 380–386.
[35] L.M. Pastrana-Martínez, S. Morales-Torres, V. Likodimos, J.L. Figueiredo, J.L. Faria, P. Falaras, A.M.T. Silva, Appl. Catal. B: Environ. 123–124 (2012) 241–256.
[36] T.D. Nguyen-Phan, V.H. Pham, E.W. Shin, H.-D. Pham, S. Kim, J.S. Chung, E.J. Kim, S.H. Hur, Chem. Eng. J. 170 (2011) 226–232.
[37] F. Wang, K. Zhang, J. Mol. Catal. A: Chem. 345 (2011) 101–107.
[38] L.M. Pastrana-Martínez, S. Morales-Torres, S.K. Papageorgiou, F.K. Katsaros, G.E. Romanos, J. Figueiredo, J.L. Faria, P. Falaras, A.M.T. Silva App, Catal. B: Environ. 142–143 (2013) 101–111.
[39] K. Rajeshwar, N.R. de Tacconi, C.R. Chenthamarakshan, Chem. Mater. 13 (2001) 2765–2782.
[40] B. Escher, R. Baumgartner, M. Koller, K. Treyer, J. Lienert, C.S. McArdell, WaterRes. 45 (2011) 75–92.
[41] M.A. Saracino, A. de Palma, G. Boncompagni, M.A. Raggi, Talanta 81 (4–5) (2010) 1547–1553.
[42] P. Calza, S. Marchisio, C. Medana, C. Baiocchi, Anal. Bioanal. Chem. 396 (2010) 1539–1550.
[43] P. Calza, C. Medana, E. Raso, V. Giancotti, C. Minero, Sci. Tot. Environ. 409 (2011) 3894–3901.
[44] C. Minero, E. Pelizzetti, R. Terzian, N. Serpone, Langmuir 10 (1994) 692–698.
[45] P. Calza, E. Pelizzetti, C. Minero, J. Appl. Electrochem. 35 (2005) 665–673.